PAPER • OPEN ACCESS

Enhancing neovascularization post-myocardial infarction through injectable hydrogel functionalized with endothelial-derived EVs

View the article online for updates and enhancements.

Biofabrication

Enhancing neovascularization post-myocardial infarction through injectable hydrogel functionalized with endothelial-derived EVs

Fabio Maiullari[1,2], Marika Milan[1,3], Maila Chirivì[3,4], Maria Grazia Ceraolo[1,3], Salma Bousselmi[2,3], Nicole Fratini[1,4], Matteo Galbiati[1,5], Orazio Fortunato[6], Marco Costantini[7] , Francesca Brambilla[5], Pierluigi Mauri[5], Dario Di Silvestre[5], Antonella Calogero[8], Tommaso Sciarra[9], Roberto Rizzi[1,8,*] and Claudia Bearzi[1,5,*]

[1] Fondazione Istituto Nazionale di Genetica Molecolare 'Romeo ed Enrica Invernizzi', Via Francesco Sforza, 35, 20122 Milan, Italy
[2] PhD Program in Cellular and Molecular Biology, Department of Biology, University of Rome 'Tor Vergata', Via della RicercaScientifica, 1, 00133 Rome, Italy
[3] Neurology Unit, Fondazione IRCCS Ca' Granda Ospedale Maggiore Policlinico, 20122 Milan, Italy
[4] Department of Molecular Medicine, Sapienza University, Viale Regina Elena, 324, 00161 Rome, Italy
[5] Institute for Biomedical Technologies, National Research Council, Via Fratelli Cervi, 93, 20054 Segrate, Milan, Italy
[6] Tumor Genomics Unit, Department of Research, IRCCS Fondazione Istituto Nazionale dei Tumori, 20133 Milan, Italy
[7] Institute of Physical Chemistry—Polish Academy of Sciences, MarcinaKasprzaka 44/52, 01-224 Warsaw, Poland
[8] Department of Medical-Surgical Sciences and Biotechnologies, Sapienza University of Rome, C.so della Repubblica 79, 04100 Latina, Italy
[9] Joint Veteran Center, Scientific Department, Army Medical Center, 00184 Rome, Italy
[*] Authors to whom any correspondence should be addressed.

E-mail: roberto.rizzi@uniroma1.it and claudia.bearzi@itb.cnr.it

Abstract

Over the past three decades, cell therapy development has fallen short of expectations, with many cellular sources demonstrating a 'Janus effect' and raising safety concerns. Extracellular vesicles (EVs), supported by advanced technologies, present a promising avenue in regenerative medicine, offering benefits such as immune tolerance and avoidance of negative aspects associated with cell transplants. Our previous research showcased enhanced and organized subcutaneous vascularization using three-dimensional bioprinted patches containing HUVEC-derived EVs in immunodeficient animal models. In this context, stress conditions on the cells of origin further boosted the EVs' neoangiogenic potential. Since neovascularization is the first regenerative target requiring restoration, the present study aims to complement our previous work by employing an injectable gelatin methacrylate (GelMA) hydrogel functionalized with HUVEC-derived EVs in a pathological condition of acute myocardial infarction. This bioactive hydrogel resulted in reduced fibrosis, improved contractility, and promoted angiogenesis, showing promise in countering tissue deterioration and addressing vascular deficits. Moreover, the molecular characterization of EVs through miRNome and proteomic analyses further supports their potential as bio-additives for hydrogel functionalization. This cell-free approach mitigates immune rejection and oncogenic risks, offering innovative therapeutic advantages.

1. Introduction

Regenerative medicine encompasses several approaches aimed at repairing or replacing damaged tissues and organs. This rapidly evolving research area embraces a wide range of strategies, including the generation of biomaterial-based scaffolds for tissue engineering, the fabrication of artificial physiological patches, and the injectable hydrogel implant [1–4]. However, at the forefront of materials science, a notable and important trend is the creation of bioactive biomaterials. The versatility of biomaterials is a key aspect, as they can be engineered to incorporate and release a variety of single or multiple biomimetic signals, including cell-derived extracellular vesicles (EVs). EVs are small immune-privileged

nanostructural particles originating from the endosomal compartment of various cell types and ranging in size from 10 to 1000 nm [5]. EVs act as cellular mediators involved in many pivotal biological processes and contain an array of components such as growth factors, proteins, cytokines, lipid fractions, nucleic acids, metabolites, and surface markers [6]. The specific composition varies depending on the cell type and can be controlled or engineered before transplantation [7]. An increasing number of studies are exploring the combination of biomaterials and EVs [8–15] recognizing its potential for advancing tissue engineering and regenerative medicine, as biological information can be transferred to regenerate the complex microarchitecture of native heterogeneous tissues and to restore biological functions while overcoming the safety limitations of whole-cell therapy [16, 17]. Interestingly, the cargo of the EVs can be manipulated to carry known loads such as genes or proteins of therapeutic interest, and further enhance their regenerative potential in tissues [18–20]. Several studies reported the efficacy of cardiac intra-wall injection of EVs in mitigating cardiac remodeling following acute myocardial infarction (AMI), providing partial evidence of their regenerative benefits [21–23]. However, in our opinion, the optimization of the therapeutic application of EVs through cargo modulation and synergizing them with a biomaterial could offer numerous advantages from biological and regenerative perspectives. While EVs present inherent limitations, such as rapid degradation and clearance in circulation, impeding sustained and targeted therapy [24], biomaterials, particularly hydrogels, serve as optimal carriers for EVs. Their exceptional biocompatibility and physicochemical properties shield EVs from harsh *in vivo* conditions, facilitating their gradual, controlled release across various tissues [25]. Moreover, the localized delivery to specific sites of interest is paramount in avoiding uncontrolled EV dispersion. In addition, the gradual release generates an EV gradient, facilitating the host's endogenous cells' colonization of the biomaterial, providing simultaneously mechanical support and promoting cell adhesion, migration, and differentiation. Additionally, EVs possess inherent adhesion molecules, enabling interaction with extracellular matrix (ECM) proteins [26], thus reducing the need for extensive biomaterial modifications. Collectively, scaffolds could enhance the clinical applications of EVs, which have been limited thus far. In this scenario, the appropriate bio-ink formulation for the stability of EVs and the storage conditions, for clinical translation, turned out to pose a significant challenge that must be addressed to advance the field of regenerative medicine [27]. In a previous work [11], we explored the potential of bioprinted Gelatin Methacrylate (GelMA) patches containing EVs derived from HUVECs, for the creation of

extra-numerary blood vessels, in immunodeficient animal models. The peculiarity in the selection of the type of EVs produced by the cells was dictated by the culture modality, in fact, the HUVECs that were starved in a hypoxic environment, showed the maximum potential for neoangiogenesis, associated with a greater enrichment in the exos ome quota compared to other subtypes of EVs. It is well known that EVs play a key role in cell communication and can influence recipient cell phenotype and cell fate. In fact, we have revealed that the effect of the massive vascular colonization of the bioprinted structures, in all its layers, is due to the significant attraction of endothelial progenitor cells (EPCs) at the site of the transplant. In the present study, we have extended the application of this concept to a pathological model of AMI. In this model, infarcted mice were treated with an injectable hydrogel functionalized with EVs derived from HUVECs cultured in starvation and hypoxia conditions. The preference for these conditions was determined by our previous study [11] in which we observed that exposure to extreme culture conditions modulates EV cargo, increasing the loading of pro-angiogenic molecules. Furthermore, EVs in bulk were used for hydrogel functionalization to prevent the loss of biological information carried by individual subpopulations of EVs. This treatment aimed to stem left ventricular pathological remodeling induced by surgical occlusion of the left descending coronary artery and restore adequate vascularization in the ischemic tissue reducing the direct consequences of the ischemic event such as exacerbated deposition of fibrosis and death of cardiomyocytes due to deprivation of blood supply.

2. Methods

2.1. Endothelial cells-derived EVs isolation

Human Umbilical Vein Endothelial Cells (HUVECs) were purchased from Thermo Fisher Scientific. The cells were expanded in Human Large Vessel Endothelial Cell Basal Medium (LVEM, M200500, Gibco). The EVs were isolated from HUVEC conditioned medium as described previously [11]. Briefly, the EVs were collected from the following two experimental conditions: (i) complete LVEM in normoxia (CM Normoxia) and (ii) serum-free LVEM in hypoxia (SM Hypoxia). The cells were cultured for 48 h in fresh medium in a standard cell culture incubator with 5% CO_2 resulting in 20% O_2 (normoxia, standard condition), or in an oxygen-controlled New Brunswick Galaxy 48 R CO_2 incubator (Eppendorf Norge AS) with a nitrogen gas line to establish 1% O_2 (hypoxia) at 5% CO_2. After 48 h, the conditioned media were collected and centrifuged at 500 g for 15 min and subsequently at 1000 g for 25 min at 4 °C to remove cell debris and organelles. Then, the supernatants were transferred into new tubes

and ultracentrifuged using an L-90 Beckman centrifuge (Beckman Instruments) equipped with a Ti-70 rotor (Beckman Instruments) at 125.000 g for 90 min at 4 °C. The obtained EVs pellets were resuspended in 100 μl of PBS and used for the subsequent experiments.

2.2. NanoSight analysis

Nanoparticle Tracking Analysis (NTA) was conducted using a NanoSight NS300 instrument (Malvern Panalytical). For each sample, five videos were recorded, each lasting 30 s. The camera level was adjusted to 15/16, and the detection threshold was set in the range of 5–7. Subsequently, the concentration and size distribution of EVs were analyzed using NTA 3.2 software.

2.3. Western blotting

The protein expression was conducted through Western blotting, utilizing the SDS–PAGE Electrophoresis System. EVs were subjected to lysis in RIPA buffer, and subsequently, 40 μg of proteins were separated on a 4%–12% Bis-Tris gel (Thermo Fisher Scientific). The membranes were then probed with primary antibodies: anti-CD9 (92726, Abcam), anti-CD63 (10628D, Invitrogen), anti-TSG101 (ab83, Abcam), anti-myeloid derived growth factor (MYDGF, 11 353-1-AP, Proteintech), anti-dysferlin (DYSF, ORB126889, Biorbyt), anti-integrin alpha 2 (ITGA2, SC-74 466, Santa Cruz Biotechnology) and anti-actin (SC-1616, Santa Cruz Biotechnology) and then with the corresponding anti-mouse (S-GENA9310, Amershan) and anti-rabbit (S-GENA934, Amershan) peroxidase-linked secondary antibodies. The detection of protein signals was carried out using a chemiluminescence method (ECL, GE Healthcare) and imaged with a MINI HD9 Western Blot Imaging System (Cleaver Scientific Ltd, United Kingdom). Quantification of the Western blots was performed using ImageJ software for analysis.

2.4. miRNome analysis

Total RNA was extracted from EVs derived from CM Normoxia and SM Hypoxia ($n = 3$) treatments using a commercial miRNeasy Mini Kit (217004, Qiagen). The purity and integrity of total RNA were analyzed using the Qubit Flex Fluorometer. Then, the samples were sequenced with NGS technology. The libraries were prepared using NEB Next Multiplex Small RNA Library Prep Set for Illumina (Set 1) (E7300, NEB) and subsequently sequenced by Illumina Novaseq6000 SE50 generating ∼20 million reads.

2.5. Proteomic analysis

Sample preparation: EV samples (CM Normoxia and SM Hypoxia, $n = 3$) were suspended in PBS after ultracentrifugation and 1% Rapigest, reconstituted in 0,1 mM NH_4HCO_3, was added to a final concentration of 0.2% v/v. The samples were heated at 95 °C for 15 min and the protein content was evaluated using the Qubit protein assay performed with Qubit4 fluorimeter (Invitrogen). The range of the total recovered protein was from 16 to 23 μg. After the digestion (supplementary information), the resulting peptides were desalted and enriched with PepClean C18 Spin Columns (Thermo Fisher Scientific), according to the manufacturer's instructions.

nLC-MS/MS analysis: each sample was analyzed in two technical replicates by LC-MS/MS platform. Eksigent nanoLC-Ultra 2D System (Eksigent) for nano liquid chromatography coupled with LTQ Orbitrap XLTM (Thermo Fisher Scientific) for MS/MS analyses. The peptides were separated with eluent gradient (supplementary information) and analyzed by tandem MS following the previously reported methods [28].

Data Processing: the experimental tandem mass spectra (MS/MS) were matched against the in-silico tryptic peptide sequences from the Homo sapiens protein database retrieved from UNIPROT (www.uniprot.org) in June 2022. Data processing was performed by Proteome Discoverer 2.5 software (Thermo Fisher Scientific), as previously reported [29].

Only peptides with a minimum peptide length of six amino acids and Rank 1 were considered, while peptide confidence was set to 'medium'. Protein grouping and strict parsimony principle were applied.

Label-free quantitation and protein–protein interaction (PPI) network analysis: the peptide spectrum match values of the identified proteins were normalized using a total signal normalization method and compared using a label-free quantification approach, as previously reported [29]. Proteins selected by LDA were processed by hierarchical clustering applying Ward's method and a Euclidean distance metric using JMP15.2 software. Finally, a PPI network was built by combining differentially expressed proteins (DEPs), and the Homo sapiens PPI network retrieved and functionally analyzed by STRING Cytoscape's app [30]; only experimentally and database-defined PPI with a score > 0.15 were considered, while GO processes, KEGG, Reactome and Wikipathways results were considered for identifying functional modules. In addition, GO processes and pathways differentially enriched were selected by LDA (*P*-value < 0.0001).

2.6. Injectable EVs-based hydrogel functionalization

Gelatin (type A3 from porcine skin) methacrylamide (GelMA) was used to produce the bioactive hydrogel as already previously described [11]. The GelMA was prepared by dissolving the gelatin in phosphate buffer (1 gr/10 ml, pH 7.5) at 50 °C and adding 0.8 ml

methacrylic anhydride dropwise under vigorous stirring (2 h). The reaction solution was diluted and dialyzed (MWCO = 2kDa) for 3 d against distilled water at 40 °C and finally freeze-dried. The sterile GelMA stock solution was prepared by dissolving 6% of GelMA w/v in 1 ml of 25 mM HEPES buffer (Sigma) and filtering the solution with 0.22 μm syringe filters. The EVs obtained in the SM Hypoxia experimental condition were employed as bioadditives to functionalize the GelMA stock solution. 4×10^9 particles/ml of hydrogel solution were loaded. The basal GelMA solution without the addition of EVs was used as the experimental control group (GelMA group). 1 mg ml^{-1} of Irgacure 2959 was used as a radical photoinitiator.

2.7. AMI and intrainfarct injection of bioactive hydrogel

C57/BL6 mice (Jackson Laboratory) were used to evaluate the cardiac regenerative potential and cardioprotective effects of the bioactive hydrogel in vivo. AMI was performed through permanent ligation of the left descending coronary artery. Two-month-old female mice underwent a previously described surgical procedure (supplementary information) [31]. Following the surgery, the animals were divided into four experimental groups ($n = 6$) (i) AMI group injected with 10 μl of saline solution, (ii) GelMA group injected with 10 μl of 6% GelMA, (iii) EVs group treated with 10 μl of EVs resuspended in saline solution, and (iv) GelMA + EVs group injected with 10 μl of EVs-based bioactive hydrogel. Transplantation was carried out using a glass Hamilton microliter syringe, by injecting the solution/hydrogel into the ischemic area right after the ligation (figure 1). The injected hydrogels were UV-crosslinked (365 nm, 200 mW cm^{-2}) for 1 min using a hand-held light gun (LED-200; Electro-lite Corp.) The SHAM experimental group consists of animals exposed to the pre-surgical preparations and post-surgical care, without the ligation of the coronary artery. The presence of functional tissue together with its effects on cardiac function was evaluated by immunofluorescence, histological assays, echocardiography, and qRT-PCR. All experiments involving animals were conducted according to the protocols of good animal experimentation under the Italian Health Minister approval no 682/2018-PR.

2.8. Echocardiographic analysis

Mice were anesthetized using 2% isoflurane inhalation and subjected to echocardiographic imaging with a VisualSonics Vevo 3100 system, employing an RMV707B scan head. M-mode echocardiography of the left ventricle was performed to evaluate the cardiac function at the following time points: day 0, 7, and 30. The following cardiac parameters were measured: fractional shortening (FS), ejection fraction (EF), left ventricular end-systolic and end-diastolic volumes (LV vol;s and LV vol;d, respectively), the thickness of the left posterior wall in systole and diastole (LVPW;s and LVPW;d), and thickness of the left anterior wall in systole and diastole (LVAW;s and LVAW;d).

2.9. Immunofluorescence assay

Heart tissues were embedded in Tissue-Tek O.C.T. compound for cryosectioning. The heart tissues were sectioned into 8 μm slices using a cryostat and processed for histological analysis. The detailed protocol was reported in the supplementary information. The sections were incubated overnight at 4 °C in a humidified chamber with primary antibodies: anti-cardiac troponin T (cTnT, 1:100, ab33589, Abcam), anti-smooth muscle actin (α-SMA, 1:200, A2547, Sigma-Aldrich), and anti-Connexin 43 (Cx43, 1:100, 3512, Cell Signaling Technology). Then, the sections were washed twice in PBS for 5 min each and incubated with fluorescent-conjugated secondary antibodies and 488-conjugated Isolectin B4 antibody (S-L2895, Sigma-Aldrich) for 2 h. Nuclei were counterstained with DAPI, and the sections were mounted using a PBS/glycerol solution.

2.10. Connexin 43 quantification

Immunofluorescence staining for Connexin 43 (Cx43) was analyzed using the image processing software ImageJ. The detailed protocol was reported in the supplementary information. Briefly, the images were converted into black and white using the 'Binary' function, and the area occupied by the Cx43 particles in the tissue sections was determined using the function 'Analyse Particles'. By analyzing these parameters, it was possible to obtain quantitative data on the abundance of Cx43 in the heart tissue samples [32].

2.11. Scar-size assessment

Heart tissue sections 8 μm thick were subjected to staining using Masson's Trichrome Stain Kit (HT15, Sigma-Aldrich). This histological technique distinctly colors the connective tissue and muscle fibers, facilitating the identification and analysis of tissue morphology and pathological changes. The procedure was carried out in accordance with the detailed instructions provided by the manufacturer. Following the staining process, the heart sections were analyzed to quantify the extent of fibrotic scarring. The scar size was expressed as a percentage, representing the ratio of the fibrotic area to the total area of the tissue section. In Masson's Trichrome staining, fibrotic areas are typically highlighted in blue, making them easily distinguishable. ImageJ software was employed to quantify these areas [33]. This quantitative analysis provided a precise assessment of the scar size, which is

Figure 1. Implantation of EVs-functionalized injectable hydrogel into the left cardiac ventricular wall. (A) Graphical representation of the acute myocardial infarction (AMI) surgical procedure and bioactive hydrogel injection into the ischemic ventricular wall. (B) Surgical procedure of AMI: (i) 8/0 nylon suture of the left anterior descending coronary artery, (ii) suture binding to create permanent coronary occlusion. (C) (i)-(iii) EVs-functionalized injectable hydrogel implant into the infarcted area on the left cardiac ventricular wall. (iv) Representative images of explanted hearts with AMI.

essential for understanding the extent of fibrosis and its impact on cardiac function.

2.12. Gene expression analysis

Heart tissues from the various experimental groups were excised 30 d post-injection for the gene expression analysis. The samples were homogenized with Tissue Ruptor and the RNA extraction was performed using a standard protocol involving the use of TRIZOL reagent (15596026, Invitrogen, Life Technologies), followed by chloroform and isopropyl alcohol precipitation. A detailed description of the extraction protocol is provided in the supplementary information section. The RNA pellet was resuspended in 30 μl of RNase-free water and its concentration was determined using a NanoDrop UV-VIS spectrophotometer. For cDNA synthesis, 1 μg of total RNA was reverse transcribed using TaqMan Fast Universal PCR Master Mix (11754–050, Superscript VILO Invitrogen). Gene expression analysis was performed via quantitative real-time PCR (qRT-PCR) on the StepOnePlus Real-Time PCR System (Applied Biosystems). The used primers are reported in table 1. Gene expression data were normalized to the Ct values of the housekeeping gene GAPDH and compared to the control groups.

For the validation of the miRNoma output, the RNA was extracted from the EVs of the two experimental conditions CM Normoxia and SM Hypoxia. After the EVs isolation, the RNA was extracted using the miRNeasy Micro Kit (217084, Qiagen). The miRNA reverse transcription was performed by miRCURY LNA RT Kit (339340, Qiagen), while the quantitative real-time PCR was performed using miRCURY LNA SYBR Green PCR Kit (339345, Qiagen). The miRNA expression data were normalized using the UniSp6 RNA spike-in.

2.13. Statistical analysis

Statistical analysis was carried out using Prism 5 (GraphPad Software, La Jolla, CA). Data are presented as mean $\pm$ SD (Standard Deviation). Differences between sample mean at each time point were evaluated with Student's t-test. P-value <0.05 was considered statistically significant.

3. Results and discussion

3.1. In-depth characterization of HUVEC-derived EVs cargo

In our prior publication, we demonstrated that the angiogenic potential of EVs derived from HUVECs can be significantly enhanced through the application of stressogenic stimuli, specifically hypoxia and starvation, to promote neovascularization *in vivo* [11]. Concurrently, we characterized EVs employing a suite of analytical techniques, including Nanoparticle Tracking Analysis, Flow Cytometry, Western Blot, Enzyme-Linked Immunosorbent Assay, and transmission electron microscopy [11]. Consequently, in the present study, we have conducted more in-depth molecular characterization of the same EVs through miRNome and proteomic analyses. This was undertaken to further investigate the potential applications of endothelial cell-derived EVs as bio-additives for hydrogel functionalization. Before these comprehensive analyses, we performed routine single-particle tracking through Nanosight analysis to confirm the size and integrity of HUVEC-derived EVs cultured under two extreme conditions: normoxia with complete medium (CM Normoxia) and hypoxia with starvation medium (SM Hypoxia). Additionally, the expression of tetraspanins proteins, such as CD9, CD63, and TSG101 was confirmed using western blot analysis (supplementary figure 1).

Table 1. Murine primer sequences for qRT-PCR analysis.

Gene symbol	Sense-forward primer	Antisense-reverse primer
Gapdh	TCCACTCATGGCAAATTCAA	TTTGATGTTAGTGGGGTCTCG
Kdr	ACGAGGAGAGAGGGTCATCT	ACACTCTCCTGCTCAGTTGG
Plgf	GTGTGCCGATAAAGACAGCC	CCTCCTTTCTGCCTTTGTCG
Vegf-a	CACGACAGAAGGAGAGCAGA	TCTCAATCGGACGGCAGTAG
Vegf-R1	TCATGTTGGATTGCTGGCAC	TGTTGGACGTTGGCTTGAAG
Tgf-β	CAACCCAGGTCCTTCCTAAA	GGAGAGCCCTGGATACCAAC
MyHC-a	CCAACACCAACCTGTCCAAG	CTCGTCGTGCATCTTCTTGG
MyHC-b	CCTGGAGAATGACAAGCAGC	GAGCTTCTTCTGCAGCTGAC
NPPA	TCTTCCTCGTCTTGGCCTTT	GACCTCATCTTCTACCGGCA
Tnf-α	CGTCGTAGCAAACCACCAAG	GGCAGAGAGGAGGTTGACTT
Il-1a	ATGTATGCCTACTCGTCGGG	CAACTCCTTCAGCAACACGG
Il-1β	TGACGGACCCCAAAAGATGA	TCTCCACAGCCACAATGAGT

miRNome analysis: the total reads evaluation revealed a notable enrichment of known as well as novel miRNAs in the SM Hypoxia group when compared to the CM Normoxia set. Specifically, the enrichment of known miRNA in the SM Hypoxia samples was 10.39%, while in the CM Normoxia group was 5.76% (figure 2(A)). The data revealed that, in conditions of oxygen deprivation, there was an increase in the production of novel miRNAs, indeed 123 miRNAs were identified in contrast to the 36 miRNAs observed in the control group (figure 2(A)). Furthermore, we observed 116 miRNAs differentially expressed in CM Normoxia and SM Hypoxia, while 390 miRNAs overlapped between the two groups (figure 2(B)). The Gene ontology analysis shows that among molecular functions (MF), cellular components (CC) and biological processes (BP), the pathways most enriched and upregulated under hypoxic conditions regarded the regulation of cell adhesion molecules, cell-to-cell junctions, adherent junctions, synaptic membranes, and postsynaptic pathways (figure 2(C)). We found 9 upregulated miRNA (miR-200a-5p, miR-574-5p, miR-let-7c-5p, miR-320b, miR-581, miR-139-5p, miR-503-5p, miR-1246, miR-320c), and 3 downregulated miRNA (miR-3615, miR-335-3p, miR-6529-5p) in SM Hypoxia vs CM Normoxia (figure 2(D)). Then, we decided to validate through qRT-PCR analysis, the expression of four of them known to be involved in cardiac (miR-574-5p and miR-139-5p) and vascular (miR-Let-7 c-5p, miR-6529-5p) dysfunctions (figure 2(E)). Specifically, the role of miR-574-5p was found to promote fibroblast-to-myofibroblast differentiation in cardiac fibrosis after myocardial infarction (MI) [34] and its upregulation to improve cell proliferation and suppress apoptotic processes in vascular smooth muscle cells (VSMCs) in patients affected by coronary artery disease (CAD) [35]. Moreover, miR-139-5p was described as a newly discovered anti-hypertrophic microRNA in cardiomyocytes by downregulating c-Jun expression *in vitro* [36]. Intriguingly, our findings demonstrated an increased expression

of miR-let-7c, a microRNA previously established to play a pivotal role in endothelial differentiation. This upregulation was associated with the enhanced transcription of key genes, including VE-cadherin, PECAM-1, and PDGFb [37]. Conversely, while miR-6529 is expressed in blood cells, its role and implications remain underexplored [38]. These findings suggest that stress conditions induce the modulation of EV's cargo uploading miRNAs that are directly involved in promoting cell adhesion and interaction, an essential process for the maintenance of tissue homeostasis.

Proteomic analysis: the proteomic analysis identified 1205 DEPs in EVs derived from CM Normoxia and 1684 DEPs from SM Hypoxia, wherein 751 were shared between the two groups (figure 3(A)). The hierarchical clustering of DEPs showed that the protein profiles are inverted between the two groups, indicating significant differences between the two conditions (figure 3(B)). DEPs were grouped into functional modules and some of them were found to be particularly affected by oxygen deprivation. The pathways upregulated in SM Hypoxia involve angiogenesis, type I collagen synthesis, vesicular trafficking, proteolytic activity, protein folding and ATP synthase mitochondrial respiration chain. Notably, the molecules upregulated in the mitochondrial pathway are ATP synthase subunits (ATP5PD, ATP5L, ATP5ME, ATP5PO) and the ATPase sarcoplasmic/endoplasmic reticulum Ca^{2+} transporter 2 (ATP2A2) in SM Hypoxia condition [39]. This upregulation could confer significant advantages to the cells targeted by EVs, enhancing their ATP production capacity and increasing their survival potential under stress conditions. Additionally, proteins involved in vesicular trafficking are also upregulated in SM hypoxia. Of particular note are clathrin light chain A (CLTA), which plays a role in microvascular niche remodelling, and flotillin-1 (FLOT1), which is involved in clathrin-independent endocytosis (CIE) [40] and regulates proteins associated with signal transduction and intracellular transport. Furthermore, the
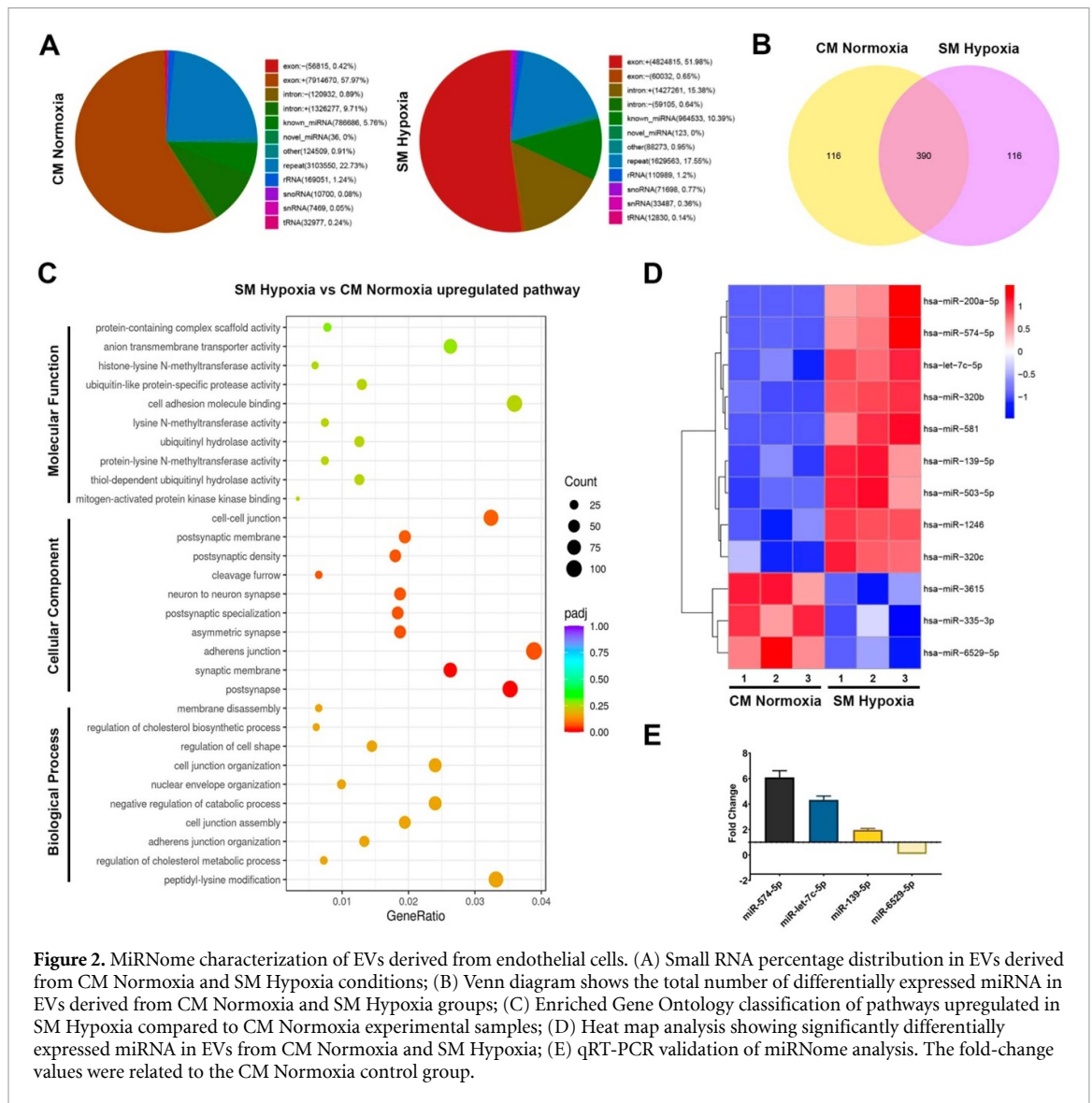
Figure 2. MiRNome characterization of EVs derived from endothelial cells. (A) Small RNA percentage distribution in EVs derived from CM Normoxia and SM Hypoxia conditions; (B) Venn diagram shows the total number of differentially expressed miRNA in EVs derived from CM Normoxia and SM Hypoxia groups; (C) Enriched Gene Ontology classification of pathways upregulated in SM Hypoxia compared to CM Normoxia experimental samples; (D) Heat map analysis showing significantly differentially expressed miRNA in EVs from CM Normoxia and SM Hypoxia; (E) qRT-PCR validation of miRNome analysis. The fold-change values were related to the CM Normoxia control group.

downregulation of apolipoproteins APOE and APOB in SM hypoxia is noteworthy, given their association with an increased risk of cardiovascular diseases when overexpressed.

Most importantly, the protein Dysferlin (DYSF), upregulated in SM Hypoxia condition, plays a significant role in angiogenic signalling and cell adhesion in proliferating endothelial cells [41]. Moreover, DYSF is involved in membrane repair in both skeletal muscle cells and cardiomyocytes and its deficiency leads to skeletal muscle necrosis and cardiomyopathy, particularly under conditions of mechanical stress [42]. In addition, the MYDGF, is an important growth factor able to enhance angiogenesis and accelerate wound healing following AMI in mice [43]. In oxygen deprivation, the expression of the Integrin alpha-2 (ITGA2) which is a cell surface protein with a crucial role in cell adhesion and cell-cell interactions was also higher (figure 3(C)). This protein interacts with specific ECM proteins like collagen, laminin,

and fibronectin and regulates cell migration and tissue development as well. The increased expression of these proteins in SM Hypoxia compared to CM Normoxia was also confirmed by western blot analysis (figure 3(D)). Collectively, these data highlight the potential of EVs to advance tissue engineering after injury. EVs actively promote tissue repair and enhance the healing process, by modulating regulatory pathways linked to angiogenesis and cellular interactions.

It is noteworthy how hypoxic and starvation conditions prompt the downregulation of pathways involved in ECM-receptor interaction and integrin-mediated signaling. This phenomenon may be attributed to the necessity, during hypoxic stress, to modulate the EVs cargo with stimulatory factors of angiogenesis, ATP synthase mitochondrial respiration, and carbohydrate-derived metabolism. Furthermore, the literature underscores the protective function of hypoxia to the expression

Figure 3. Proteomic Analysis of EVs derived from endothelial cells. (A) A Venn diagram shows the total number of proteins identified by EVs derived from CM Normoxia and SM Hypoxia conditions; (B) Heat map analysis showing differentially expressed proteins (DEPs) between CM Normoxia and SM Hypoxia; (C) protein–protein interaction (PPI) network analysis. DEPs were classified into 35 functional modules. Node colour code indicates in red and in blue light proteins up- and downregulated, respectively. (D) Validation of proteomic analysis through western blot analysis for Dysferlin, MYDGF and Integrin a2 quantified as optical density (OD) of protein bands normalized to Actin. Error bars represent ±SEM. Student's t test, $^*p < 0.05$, $^{**}p < 0.01$.

of ECM remodeling—related genes, such as TGF-β, in endothelial cells, shields the heart and aorta from pressure overload [44], influencing cell adhesion, proliferation, and differentiation as well [45]. Additionally, the hypoxia-induced downregulation of the Wnt/β-catenin pathway, pivotal in the regulation of genes associated with cell proliferation and adhesion, collagen deposition, and ECM remodeling, could provide further support to these findings [46, 47].

3.2. Bioactive hydrogel characterization
GelMA hydrogels—pristine or loaded with EVs—were characterized using SEM and mechanical testing

to determine their internal morphology and Young's moduli (supplementary figure 2). The detailed methods were reported in the supplementary information. SEM analysis revealed that both matrices displayed a similar intricate network of pores. At high magnification, noticeable differences in surface morphology emerged: hydrogels loaded with EVs exhibited a bumpy surface attributable to the nanoparticles themselves anchored on the polymer surface, whereas the EV-free samples displayed a smooth and regular surface. Additionally, the spatial distribution of EVs appeared uniform throughout the biopolymer matrix. Additionally, the two GelMA hydrogel groups were subjected to mechanical compression testing to

Figure 4. Echocardiographic analysis of transplanted mice. (A) Representative M-mode images from a short-axis view of the left ventricle were obtained using the RMV 707B scanhead. The measured parameters are shown in the upper image; (B) Echocardiographic measurements at day 7 (T7) and day 30 (T30). The SHAM reference control group value was reported for each parameter. Fractional shortening (FS), ejection fraction (EF), left ventricular end-systolic/diastolic volume (LV vol; s and LV vol; d), left posterior wall thickness in systole and diastole (LVPW;s and LVPW;d), left anterior wall thickness in systole and diastole (LVAW;s and LVAW;d). $N = 5$ mice for each experimental group were analyzed. Error bars represent ±SEM. Student's t test, $*p < 0.05$, $**p < 0.01$, $***p < 0.001$.
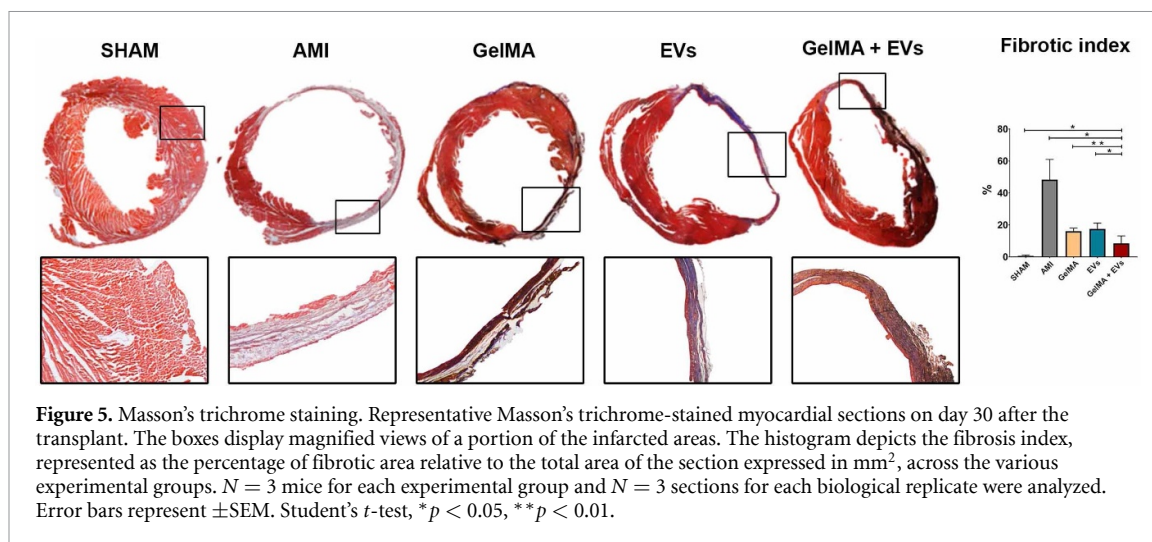
assess their behavior under load. Such investigation confirmed that the addition of EVs—at least for the concentration used in this study—to a 6% w/v GelMA solution did not alter the mechanical response of the gels, which exhibited in both cases a Young's modulus of around 2 kPa. This result underscores that the incorporation of nanostructured vesicles in the bioink does not alter the processability and stability of the gels. Accordingly, the material's ability to support colonization and differentiation by host-derived cells was not compromised by functionalization.

3.3. Bioactive hydrogel effects on infarcted hearts performance

In this study which explores the therapeutic potential of EVs-based functionalized hydrogels, we assessed the bioactivity of GelMA encapsulating the EVs derived from SM hypoxia treatment on myocardial recovery post-AMI in a mouse model. Upon coronary ligation, we stratified the animals into four defined cohorts: (i) SHAM control group; (ii) AMI control; (iii) GelMA injection; (iv) EVs injection; and (v) GelMA + EVs injection. An echocardiographic evaluation was performed to reveal the bioactive hydrogel effects on cardiac function (figure 4(A)). As expected for infarcted mice, from day 0 to day 7 and through day 30 post-infarction, both the fractional shortening (FS) and ejection fraction (EF)—two critical parameters gauging cardiac performance—displayed a marked decline, reflecting the advancement of pathological cardiac conditions. However,

the animals treated with the EVs-functionalized hydrogel displayed significant improvements in FS and EF between day 7 and day 30 compared to the experimental groups treated with Saline, GelMA, or EVs alone (figure 4(B)). The FS and EF values in the GelMA + EVs group were increased, approaching values more similar to those of the SHAM control group. Specifically, on day 7, the group treated with GelMA + EVs showed a notable increase in FS and EF values compared to the group that received only the EVs. This improvement was also statistically significant on day 30, when compared also to the AMI and GelMA cohorts. Another important aspect observed was the modulation of left ventricular volume (LV vol). The increase in LV vol is typically a direct result of decreased cardiac wall tonicity, leading to progressive dilated cardiomyopathy. The obtained results indicated a significant reduction in left ventricular volume in systole (LV vol;s) on days 7 and 30 and in diastole (LV vol;d) on day 30 for GelMA + EVs group compared to the other conditions. While the reduction of LV vol;d in the GelMA + EVs group was statistically significant on day 30 only when compared to the AMI group. Furthermore, a significant boost was also observed in the thickness of the posterior left ventricular wall, both in systole and diastole (LVPW;s and LVPW;d) at day 30, in the GelMA + EVs group compared to the GelMA group, and compared to the AMI group only in systole. Finally, the thickness of the left anterior ventricular wall in systole (LVAW;s) was found to be

Figure 5. Masson's trichrome staining. Representative Masson's trichrome-stained myocardial sections on day 30 after the transplant. The boxes display magnified views of a portion of the infarcted areas. The histogram depicts the fibrosis index, represented as the percentage of fibrotic area relative to the total area of the section expressed in mm^2, across the various experimental groups. $N = 3$ mice for each experimental group and $N = 3$ sections for each biological replicate were analyzed. Error bars represent $\pm$SEM. Student's *t*-test, $^*p < 0.05$, $^{**}p < 0.01$.

significantly expanded after 30 d post-implantation in the two experimental groups in which the animals were injected with the hydrogel, compared to the animals with only AMI (figure 4(B)). In conclusion, the echocardiographic data reveal that the animals treated with the bioactive hydrogel (GelMA + EVs) exhibited enhanced cardiac performance after 30 d. This improvement was evidenced by increased shortening and ejection fractions, indicative of better heart function. Additionally, there was a notable reduction of dilated cardiomyopathy-associated manifestation, as shown by the reduced ventricular volume observed at both 7 and 30 d. Furthermore, pathological remodeling of the ventricular wall was diminished, as evidenced by the increased thickness of the posterior and anterior ventricular walls.
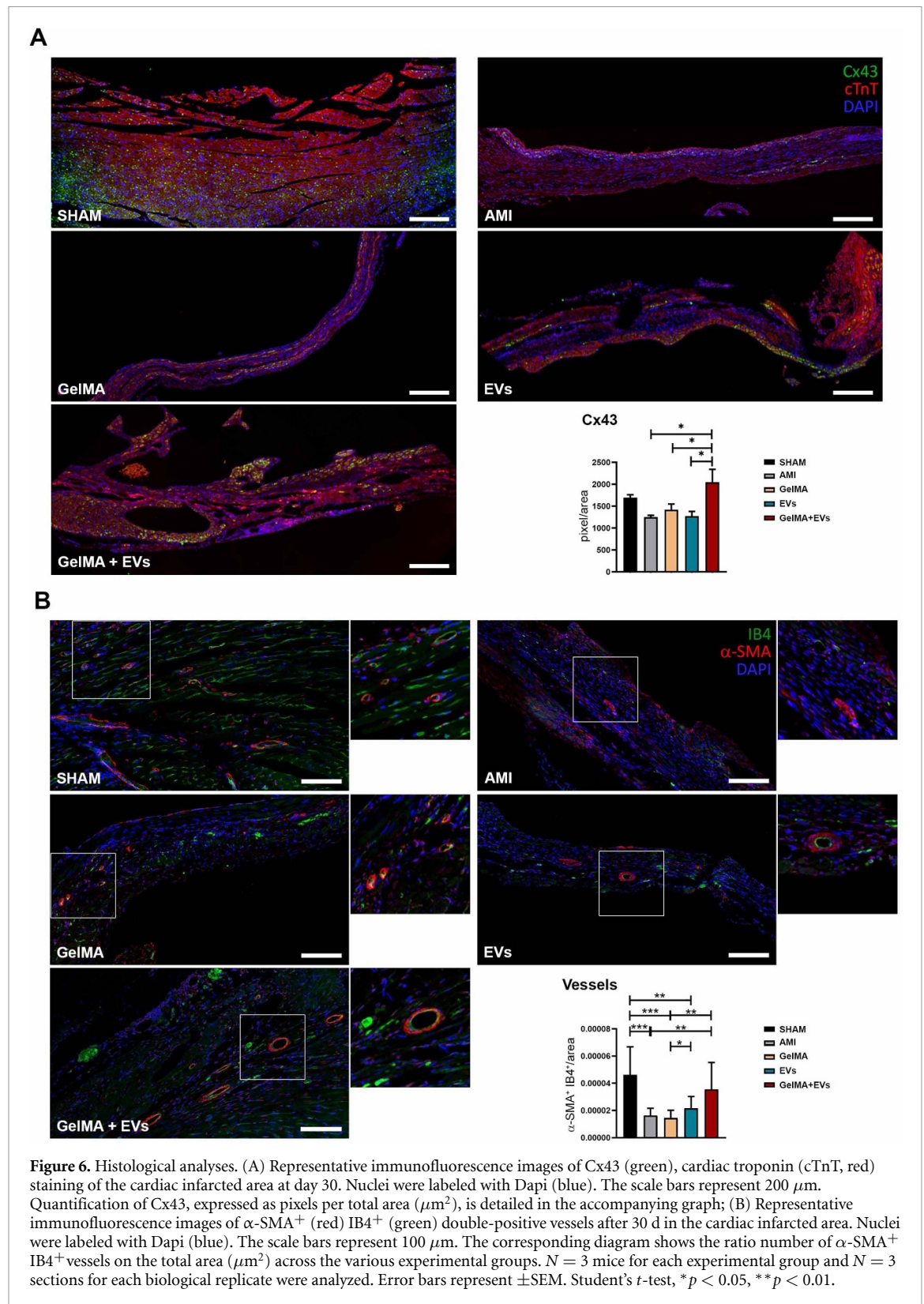
3.4. Regenerative effects of bioactive hydrogels on infarcted myocardium

Masson's Trichrome staining was used to delineate the pathological accumulation of connective tissue typically observed after an ischemic event. This accumulation contributes to aberrant remodelling of the ventricular wall, which is reflected in diminished contractile capacity.

As expected, the mice that underwent AMI exhibited a fibrotic index exceeding 15% in the left ventricular wall. In contrast, the SHAM control group displayed negligible fibrosis values, primarily attributable to physiological perivascular fibrosis (figure 5). Specifically, the group treated with the bioactive hydrogel exhibited a statistically significant decrease in abnormal collagen deposition compared to the other experimental cohorts. This suggests that the hydrogel functions as an anchoring matrix for EVs, preventing their dispersion and enhancing their localized regenerative impact (figure 5). Additionally, administering GelMA alone also led to a diminished fibrotic response compared to AMI group. This effect might be attributed to the mechanical
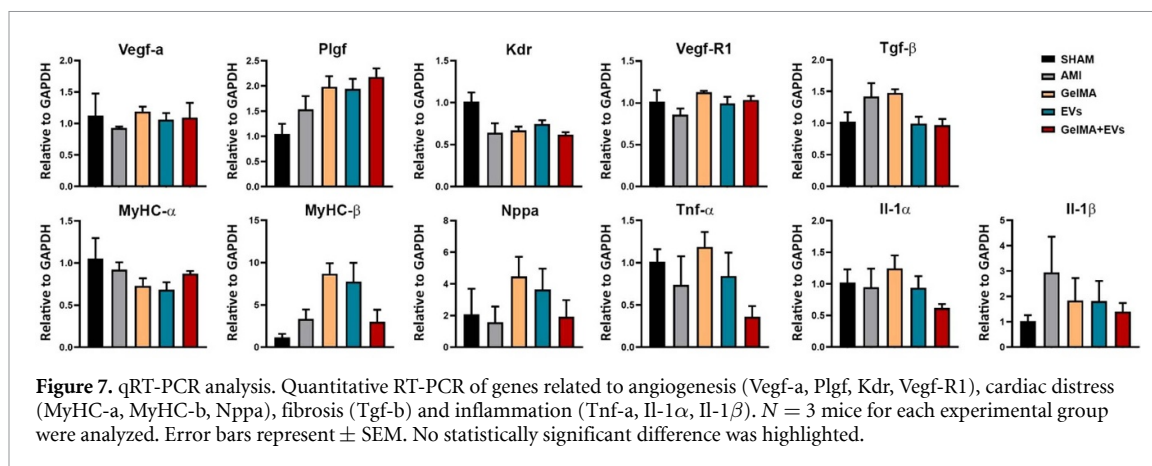
stimuli of crosslinked GelMA, thereby inhibiting the further secretion of collagen by the resident stromal cells. The synergistic effect of GelMA's inhibitory influence and the regenerative, tissue-preserving properties of EVs, specifically targeted to the cardiac muscle and the vasculature, could explain the observed reduction in ventricular wall remodelling (figure 5). This histological result is reflected in the improvement of cardiac function with an increased contractile capacity of the myocardium, as evidenced in the echocardiographic evaluations previously shown.

The heart functionality and the myocardium morphology are directly correlated with the uniform distribution of Connexin 43 (Cx43), which is crucial for the regulation of myocardial gap junctions. Additionally, the density of arterioles plays a significant role, facilitating the adequate delivery of growth factors, nutrients, and oxygen. This is particularly important given the myocardium's high metabolic demand and its continuous contractile activity. As expected, the induction of AMI markedly compromised these two features in the ventricular ischemic region. However, the obtained results indicated that in the group receiving GelMA + EVs transplantation, the tissue area-normalized expression of Cx43 was reinstated to levels akin to those observed in the SHAM group. Furthermore, the increased Cx43 expression was statistically significant in comparison to the three control groups AMI, GelMA, and EVs (figure 6(A)). The data also revealed that the different transplantation types significantly influenced the amount of alpha-smooth muscle actin (α-SMA) and Isolectin B4 double-positive vessels. Notably, the group receiving GelMA + EVs transplantation exhibited a statistically significant increase in vessel amount compared to both the AMI and GelMA groups (figure 6(B)). In contrast, the AMI, GelMA and EVs groups demonstrated a marked decrease in vessel numbers relative to the SHAM control

Figure 6. Histological analyses. (A) Representative immunofluorescence images of Cx43 (green), cardiac troponin (cTnT, red) staining of the cardiac infarcted area at day 30. Nuclei were labeled with Dapi (blue). The scale bars represent 200 μm. Quantification of Cx43, expressed as pixels per total area (μm^2), is detailed in the accompanying graph; (B) Representative immunofluorescence images of α-SMA$^+$ (red) IB4$^+$ (green) double-positive vessels after 30 d in the cardiac infarcted area. Nuclei were labeled with Dapi (blue). The scale bars represent 100 μm. The corresponding diagram shows the ratio number of α-SMA$^+$ IB4$^+$ vessels on the total area (μm^2) across the various experimental groups. $N = 3$ mice for each experimental group and $N = 3$ sections for each biological replicate were analyzed. Error bars represent $\pm$SEM. Student's t-test, $^*p < 0.05$, $^{**}p < 0.01$.

group. This finding confirms that the induction of AMI led to a substantial loss of blood vessels in the ischemic area, thereby reducing blood supply. The angiogenic efficacy of EVs was further underscored by their ability to maintain an adequate number of blood vessels, even in the experimental group treated solely with EVs (figure 6(B)). This outcome highlights the potent angiogenic properties of endothelial cell-derived EVs, whose bioactivity is maximized by the site-specific anchoring provided by the hydrogel. This synergistic effect of EVs and hydrogel in vascular tissue preservation, in the ischemic tissues, aligns

Figure 7. qRT-PCR analysis. Quantitative RT-PCR of genes related to angiogenesis (Vegf-a, Plgf, Kdr, Vegf-R1), cardiac distress (MyHC-a, MyHC-b, Nppa), fibrosis (Tgf-b) and inflammation (Tnf-a, Il-1α, Il-1β). $N = 3$ mice for each experimental group were analyzed. Error bars represent $\pm$ SEM. No statistically significant difference was highlighted.

with the findings from our previous research [11] which demonstrated the significant angiogenic capacity of GelMA functionalized with EVs, however, in a physiological context.

Gene expression analysis was conducted 30 d post-transplantation to explore the underlying molecular mechanisms. Although no statistically significant differences in gene expression were observed, which could be attributed to gene expression stabilization after 30 d, notable changes were detected. Specifically, there was an upregulation of genes associated with angiogenesis (Vegf-a, Plgf, Vegf-R1) in the GelMA + EVs group. Additionally, markers indicative of cardiac distress (Nppa, MyHC-β), fibrosis (Tgf-β), and inflammation (Tnf-α, Il-1α, Il-1β) exhibited downregulation (figure 7) in the animals treated with the bioactive hydrogel. Overall, these data are consistent with our earlier *in vitro* findings, which demonstrated that EVs from endothelial cells subjected to starvation and hypoxia promote the differentiation of human EPCs. This was attested by the increased expression of CD31, VEGFR2, and CD45. Additionally, when EPCs were seeded onto EV-loaded constructs, they formed tubular, vessel-like structures [11].

The additional results collectively highlight the effectiveness of EVs-functionalized GelMA in enhancing myocardial tissue health. This combination not only reduces fibrosis but also improves contractility and promotes angiogenesis. The underlying mechanism likely involves the hydrogel's ability to create a favourable microenvironment, maintaining tissue homeostasis and enhancing regenerative processes after injury, leveraging the therapeutic properties of the EVs.

4. Conclusion

Cell-free regenerative strategies are gaining prominence due to their ability to circumvent the adverse effects associated with the use of immune-competent or potentially oncogenic cell populations [48–50]. These approaches offer a significant therapeutic advantage by avoiding immune rejection and the oncogenic risks inherent in tissue transplantation, focusing instead on harnessing the beneficial signals produced by cells [51, 52]. Furthermore, they address the challenge of transplant engraftment, particularly in ischemic areas where poor nutrient availability can impede the survival and integration of live cells, thus limiting tissue repair and organ function restoration [53, 54]. Our innovative approach, employing a bioactive hydrogel in a myocardial infarction model, has demonstrated remarkable efficacy in countering tissue deterioration. This strategy effectively preserves and enhances the formation of new blood vessels, thereby preventing the decline of cardiac functions. The use of an injectable hydrogel, augmented with natural bio-additives like EVs derived from HUVECs, has proven to be a versatile tool for transplantation in various physiological areas requiring vascular support. This immune-privileged method could be particularly beneficial, even in genetic disorders like diabetes, which predominantly cause vascular deficits.

EVs, as lipid bilayer-enclosed particles secreted by cells, play a crucial role in intercellular communication, carrying proteins, nucleic acids, and other biological components. The field of regenerative medicine has traditionally utilized natural, hybrid, or composite polymers in biomaterial applications. However, the future promises to integrate naturalized additives, potentially leading to significant advancements in regenerative capabilities while maintaining safety standards. This approach could represent a significant leap forward in regenerative medicine, offering a safer, more effective alternative to traditional cell-based therapies.

Data availability statement

The data that support the findings of this study are available upon reasonable request from the authors.

Acknowledgments

ORCID iDs

Marco Costantini ⬤ https://orcid.org/0000-0003-2756-5872
Claudia Bearzi ⬤ https://orcid.org/0000-0002-8218-9833

References

[1] de Wit R J J, van Dis D J, Bertrand M E, Tiemessen D, Siddiqi S, Oosterwijk E and Verhagen A F T M 2023 Scaffold-based tissue engineering: supercritical carbon dioxide as an alternative method for decellularization and sterilization of dense materials *Acta Biomater.* **155** 323–32

[2] Ilhan E, Ulag S, Sahin A, Yilmaz B K, Ekren N, Kilic O, Sengor M, Kalaskar D M, Oktar F N and Gunduz O 2021 Fabrication of tissue-engineered tympanic membrane patches using 3D-Printing technology *J. Mech. Behav. Biomed. Mater.* **114** 104219

[3] Liu G, Zhou Y, Zhang X and Guo S 2022 Advances in hydrogels for stem cell therapy: regulation mechanisms and tissue engineering applications *J. Mater. Chem.* B **10** 5520–36

[4] Ji R, Hao Z, Wang H, Li X, Duan L, Guan F and Ma S 2023 Application of injectable hydrogels as delivery systems in spinal cord injury *Gels* **9** 907

[5] Tian Y *et al* 2020 Quality and efficiency assessment of six extracellular vesicle isolation methods by nano-flow cytometry *J. Extracell. Ves.* **9** 1697028

[6] Doyle L M and Wang M Z 2019 Overview of extracellular vesicles, their origin, composition, purpose, and methods for exosome isolation and analysis *Cells* **8** 727

[7] Pegtel D M and Gould S J 2019 Exosomes *Annu. Rev. Biochem.* **88** 487–514

[8] Born L J, McLoughlin S T, Dutta D, Mahadik B, Jia X, Fisher J P and Jay S M 2022 Sustained released of bioactive mesenchymal stromal cell-derived extracellular vesicles from 3D-printed gelatin methacrylate hydrogels *J. Biomed. Mater. Res.* A **110** 1190–8

[9] Chen P *et al* 2019 Desktop-stereolithography 3D printing of a radially oriented extracellular matrix/mesenchymal stem cell exosome bioink for osteochondral defect regeneration *Theranostics* **9** 2439–59

[10] Kang Y, Xu J, Meng L, Su Y, Fang H, Liu J, Cheng Y Y, Jiang D, Nie Y and Song K 2023 3D bioprinting of dECM/Gel/QCS/nHAp hybrid scaffolds laden with mesenchymal stem cell-derived exosomes to improve angiogenesis and osteogenesis *Biofabrication* **15** 024103

[11] Maiullari F *et al* 2021 *In vivo* organized neovascularization induced by 3D bioprinted endothelial-derived extracellular vesicles *Biofabrication* **13** 035014

[12] Sun Y, Zhang B, Zhai D and Wu C 2021 Three-dimensional printing of bioceramic-induced macrophage exosomes: immunomodulation and osteogenesis/angiogenesis *NPG Asia Mater.* **13** 72

[13] Yerneni S S, Whiteside T L, Weiss L E and Campbell P G 2019 Bioprinting exosome-like extracellular vesicle microenvironments *Bioprinting* **13** e00041

[14] Yerneni S S, Adamik J, Weiss L E and Campbell P G 2021 Cell trafficking and regulation of osteoblastogenesis by extracellular vesicle associated bone morphogenetic protein 2 *J. Extracell. Ves.* **10** e12155

[15] Yerneni S S, Lathwal S, Shrestha P, Shirwan H, Matyjaszewski K, Weiss L, Yolcu E S, Campbell P G and Das S R 2019 Rapid On-demand extracellular vesicle augmentation with versatile oligonucleotide tethers *ACS Nano* **13** 10555–65

[16] Jiao K L C, Basu S, Raveendran N, Nakano T, Ivanovski S and Han P 2023 Bioprinting extracellular vesicles as a "cell-free" regenerative medicine approach *Extracell. Ves. Circ. Nucl. Acids* **4** 218–39

[17] Pulido-Escribano V, Torrecillas-Baena B, Dorado G, Gálvez-Moreno M Á, Camacho-Cardenosa M and Casado-Díaz A 2023 Combination of biomaterials and extracellular vesicles from mesenchymal stem-cells: new therapeutic strategies for skin-wound healing *Appl. Sci.* **13** 2702

[18] Han Y, Jones T W, Dutta S, Zhu Y, Wang X, Narayanan S P, Fagan S C and Zhang D 2021 Overview and update on methods for cargo loading into extracellular vesicles *Processes* **9** 356

[19] Joshi B S, Ortiz D and Zuhorn I S 2021 Converting extracellular vesicles into nanomedicine: loading and unloading of cargo *Mater. Today Nano* **16** 100148

[20] Rädler J, Gupta D, Zickler A and Andaloussi S E 2023 Exploiting the biogenesis of extracellular vesicles for bioengineering and therapeutic cargo loading *Mol. Ther.* **31** 1231–50

[21] Zheng Y L, Wang W D, Cai P Y, Zheng F, Zhou Y F, Li M M, Du J-R, Lin S and Lin H-L 2022 Stem cell-derived exosomes in the treatment of acute myocardial infarction in preclinical animal models: a meta-analysis of randomized controlled trials *Stem Cell Res. Ther.* **13** 151

[22] Liu Y, Wang M, Yu Y, Li C and Zhang C 2023 Advances in the study of exosomes derived from mesenchymal stem cells and cardiac cells for the treatment of myocardial infarction *Cell Commun. Signaling* **21** 202

[23] Cheng P, Wang X, Liu Q, Yang T, Qu H and Zhou H 2023 Extracellular vesicles mediate biological information delivery: a double-edged sword in cardiac remodeling after myocardial infarction *Front. Pharmacol.* **14** 1067992

[24] Xing H, Zhang Z, Mao Q, Wang C, Zhou Y, Zhou X, Ying L, Xu H, Hu S and Zhang N 2021 Injectable exosome-functionalized extracellular matrix hydrogel for metabolism balance and pyroptosis regulation in intervertebral disc degeneration *J. Nanobiotechnol.* **19** 264

[25] Lazar S, Mor S, Chen J, Hao D and Wang A 2021 Bioengineered extracellular vesicle-loaded bioscaffolds for therapeutic applications in regenerative medicine. Extracellular vesicles and circulating nucleic acids *Extracell Ves. Circ. Nucl. Acids* **2** 175–8

[26] Hao D, Swindell H S, Ramasubramanian L, Liu R, Lam K S, Farmer D L and Wang A 2020 Extracellular matrix mimicking nanofibrous scaffolds modified with mesenchymal stem cell-derived extracellular vesicles for improved vascularization *Front. Bioeng. Biotechnol.* **8** 633

[27] Ozkocak D C, Phan T K and Poon I K H 2022 Translating extracellular vesicle packaging into therapeutic applications *Front. Immunol.* **13** 946422

[28] De Palma A, Agresta A M, Viglio S, Rossi R, D'Amato M, Di Silvestre D, Mauri P and Iadarola P 2021 A shotgun proteomic platform for a global mapping of lymphoblastoid cells to gain insight into Nasu-Hakola disease *Int. J. Mol. Sci.* **22** 9959

[29] Di Silvestre D *et al* 2023 The protein network in subcutaneous fat biopsies from patients with AL amyloidosis: more than diagnosis? *Cells* **12** 699

[30] Doncheva N T, Morris J H, Gorodkin J and Jensen L J 2019 Cytoscape StringApp: network analysis and visualization of proteomics data *J. Proteome Res.* **18** 623–32

[31] Bearzi C, Gargioli C, Baci D, Fortunato O, Shapira-Schweitzer K, Kossover O, Latronico M V G, Seliktar D, Condorelli G and Rizzi R 2014 PlGF–MMP9-engineered iPS cells supported on a PEG–fibrinogen hydrogel scaffold possess an enhanced capacity to repair damaged myocardium *Cell Death Dis.* **5** e1053

[32] Milan M *et al* 2018 Givinostat reduces adverse cardiac remodeling through regulating fibroblasts activation *Cell Death Dis.* **9** 108

[33] Stirm M *et al* 2021 A scalable, clinically severe pig model for Duchenne muscular dystrophy *Dis. Models Mech.* **14** dmm049285

[34] Cui J, Qi S, Liao R, Su D, Wang Y and Xue S 2020 MiR-574-5p promotes the differentiation of human cardiac fibroblasts via regulating ARID3A *Biochem. Biophys. Res. Commun.* **521** 427–33

[35] Lai Z, Lin P, Weng X, Su J, Chen Y, He Y, Wu G, Wang J, Yu Y and Zhang L 2018 MicroRNA-574-5p promotes cell growth of vascular smooth muscle cells in the progression of coronary artery disease *Biomed. Pharmacother.* **97** 162–7

[36] Ming S, Shui-Yun W, Wei Q, Jian-Hui L, Ru-Tai H, Lei S, Mei J, Hui W and Ji-zheng W 2018 miR-139-5p inhibits isoproterenol-induced cardiac hypertrophy by targetting c-Jun *Biosci. Rep.* **38** BSR20171430

[37] Coppola A *et al* 2014 Cardiomyogenesis is controlled by the miR-99a/let-7c cluster and epigenetic modifications *Stem Cell Res.* **12** 323–37

[38] Ioannidis J and Donadeu F X 2018 Comprehensive analysis of blood cells and plasma identifies tissue-specific miRNAs as potential novel circulating biomarkers in cattle *BMC Genomics* **19** 243

[39] Li D *et al* 2023 AMPK activator-treated human cardiac spheres enhance maturation and enable pathological modeling *Stem Cell Res. Ther.* **14** 322

[40] Dam D H M, Jelsma S A, Yu J M, Liu H, Kong B and Paller A S 2020 Flotillin and AP2A1/2 promote IGF-1 receptor association with clathrin and internalization in primary human keratinocytes *J. Investigative Dermatol.* **140** 1743–52.e4

[41] Sharma A, Yu C, Leung C, Trane A, Lau M, Utokaparch S, Shaheen F, Sheibani N and Bernatchez P 2010 A new role for the muscle repair protein dysferlin in endothelial cell adhesion and angiogenesis *Arteriosclerosis Thrombosis Vasc. Biol.* **30** 2196–204

[42] Han R, Bansal D, Miyake K, Muniz V P, Weiss R M and McNeil P L 2007 Dysferlin-mediated membrane repair protects the heart from stress-induced left ventricular injury *J. Clin. Invest.* **117** 1805–13

[43] Korf-Klingebiel M *et al* 2015 Myeloid-derived growth factor (C19orf10) mediates cardiac repair following myocardial infarction *Nat. Med.* **21** 140–9

[44] Wei H *et al* 2012 Endothelial expression of hypoxia-inducible factor 1 protects the murine heart and aorta from pressure overload by suppression of TGF-β signaling *Proc. Natl Acad. Sci. USA* **109** E841–50

[45] Tzavlaki K and Moustakas A 2020 TGF-β Signaling *Biomolecules* **10** 487

[46] Verras M, Papandreou I, Lim A L and Denko N C 2008 Tumor hypoxia blocks Wnt processing and secretion through the induction of endoplasmic reticulum stress *Mol. Cell Biol.* **28** 7212–24

[47] Rodriguez D, Watts D, Gaete D, Sormendi S and Wielockx B 2021 Hypoxia pathway proteins and their impact on the blood vasculature *Int. J. Mol. Sci.* **22** 9191

[48] Cui L, Saeed Y, Li H and Yang J 2022 Regenerative medicine and traumatic brain injury: from stem cell to cell-free therapeutic strategies *Regen. Med.* **17** 37–53

[49] Moghadasi S *et al* 2021 A paradigm shift in cell-free approach: the emerging role of MSCs-derived exosomes in regenerative medicine *J. Transl. Med.* **19** 302

[50] Safari B, Aghazadeh M, Davaran S and Roshangar L 2022 Exosome-loaded hydrogels: a new cell-free therapeutic approach for skin regeneration *Eur. J. Pharm. Biopharm.* **171** 50–59

[51] Petrus-Reurer S, Romano M, Howlett S, Jones J L, Lombardi G and Saeb-Parsy K 2021 Immunological considerations and challenges for regenerative cellular therapies *Commun. Biol.* **4** 798

[52] Platt J L, Cascalho M and Piedrahita J A 2018 Xenotransplantation: progress along paths uncertain from models to application *ILAR J.* **59** 286–308

[53] Arjmand B, Abedi M, Arabi M, Alavi-Moghadam S, Rezaei-Tavirani M, Hadavandkhani M, Tayanloo-Beik A, Kordi R, Roudsari P P and Larijani B 2021 Regenerative medicine for the treatment of ischemic heart disease; status and future perspectives *Front. Cell Dev. Biol.* **9** 704903

[54] Gu Y, Rampin A, Alvino V V, Spinetti G and Madeddu P 2021 Cell therapy for critical limb ischemia: advantages, limitations, and new perspectives for treatment of patients with critical diabetic vasculopathy *Curr. Diabetes Rep.* **21** 11